

Article

# Hurricane Wind Speed Estimation Using WindSat 6 and 10 GHz Brightness Temperatures

Lei Zhang <sup>1,2</sup>, Xiao-bin Yin <sup>2,3,4,\*</sup>, Han-qing Shi <sup>1</sup> and Zhen-zhan Wang <sup>2,3</sup>

<sup>1</sup> Institute of Meteorology and Oceanography, PLA University of Science and Technology, Nanjing 211101, China; zlei\_best@hotmail.com (L.Z.); mask1000@126.com (H.S.)

<sup>2</sup> Key Laboratory of Microwave Remote Sensing, Chinese Academy of Sciences, Beijing 100190, China; wangzhenzhan@mirslab.cn

<sup>3</sup> National Space Science Center, Chinese Academy of Sciences, Beijing 100190, China

<sup>4</sup> Beijing Piesat Information Technology Co., Ltd., Beijing 100190, China

\* Correspondence: yinxiaobin@mirslab.cn; Tel.: +86-10-6258-2844

Academic Editors: Xiaofeng Li and Prasad S. Thenkabail

Received: 4 August 2016; Accepted: 23 August 2016; Published: 31 August 2016

**Abstract:** The realistic and accurate estimation of hurricane intensity is highly desired in many scientific and operational applications. With the advance of passive microwave polarimetry, an alternative opportunity for retrieving wind speed in hurricanes has become available. A wind speed retrieval algorithm for wind speeds above 20 m/s in hurricanes has been developed by using the 6.8 and 10.7 GHz vertically and horizontally polarized brightness temperatures of WindSat. The WindSat measurements for 15 category 4 and category 5 hurricanes from 2003 to 2010 and the corresponding H\*wind analysis data are used to develop and validate the retrieval model. In addition, the retrieved wind speeds are also compared to the Remote Sensing Systems (RSS) global all-weather product and stepped-frequency microwave radiometer (SFMR) measurements. The statistical results show that the mean bias and the overall root-mean-square (RMS) difference of the retrieved wind speeds with respect to the H\*wind analysis data are 0.04 and 2.75 m/s, respectively, which provides an encouraging result for retrieving hurricane wind speeds over the ocean surface. The retrieved wind speeds show good agreement with the SFMR measurements. Two case studies demonstrate that the mean bias and RMS difference are 0.79 m/s and 1.79 m/s for hurricane Rita-1 and 0.63 m/s and 2.38 m/s for hurricane Rita-2, respectively. In general, the wind speed retrieval accuracy of the new model in hurricanes ranges from 2.0 m/s in light rain to 3.9 m/s in heavy rain.

**Keywords:** polarimetric microwave radiometer; sea surface wind retrieval; WindSat; H\*wind analysis data

## 1. Introduction

Passive microwave remote sensing is an important tool for studying atmospheric and oceanographic processes and can provide both daytime and nighttime observations of geophysical parameters [1], such as atmospheric water vapor, cloud liquid water, rain rate, sea surface temperature, sea surface wind, and sea ice. This tool can provide scientists and forecasters with vital information for understanding and studying global weather and climate change. The first Special Sensor Microwave Imager (SSM/I) aboard the Defense Meteorological Satellite Program (DMSP) was launched in July 1987 [2], making it possible to obtain the global ocean surface wind from a spaceborne passive microwave instrument [3]. Since then, a successive dataset of wind speed has been obtained from the passive microwave radiometry [3–5].

Algorithms [3,6–9] have been developed for passive microwave radiometry that are able to retrieve the wind speeds of low to moderate winds in no-rain areas with a good degree of accuracy.

However, these algorithms seem to break down completely when the scenes are under severe weather conditions, including both high winds and precipitation. It is difficult to measure wind speeds in these conditions because the physics of ocean surface remote sensing is still poorly understood under these weather conditions. Intense rain not only influences the atmospheric attenuation but also changes the sea surface dielectric properties in a complicated manner [10,11]. Thus, it is very difficult to accurately model brightness temperatures in these situations. Fortunately, the brightness temperature (TB) acquired at the lower frequencies, such as the L-band and C-band, are far from saturation, which is the physical reason that researchers can “see” the ocean surface and derive its properties [11,12]. A new capability for ocean surface wind speed retrieval is performed using the L-band brightness temperatures provided by the Soil Moisture and Ocean Salinity (SMOS) mission [11]. The study [11] shows that the L-band ocean emissivity dependence with wind speed appears to be less sensitive to roughness and foam changes than at the higher C-band microwave frequencies. A physical method is developed to retrieve sea surface temperature and wind speed for hurricane predictions in [13]. In [13], the effects of precipitation emission and scattering on the measurements are both taken into account. However, the used ocean microwave emissivity model is performed in clear sky conditions and at low wind speeds (smaller than 25 m/s). Hence, the performance of the model needs to be further tested at high wind speeds and intensely rainy conditions. In addition, the C-band H-polarization TBs provided by AMSR-E and AMSR2 are used to retrieve wind speed in hurricanes using the small slope approximation method and an ocean surface roughness spectrum [14]. In [14], the retrieved wind speeds are vulnerable to rain because the model does not account for the effects of absorption and scattering caused by rain.

It is very difficult to accurately model brightness temperatures in rain because of the high variability in rainy atmospheres. Thus, the statistical algorithm seems to be a good candidate for retrieval of wind speeds in this situation. For accurate radiometer retrievals of wind speeds under rainy conditions, channel combination methods at different frequencies have been used to retrieve wind speeds [10,12,15,16]. The core of these algorithms makes it possible to reduce the signal coming from rain without considerably reducing the wind speed signal. Such a technique has been employed successfully for wind speed retrieval with the airborne microwave polarimetry. In addition, an artificial neural network technique has been used to derive the relationship between the AMSR2 TBs and sea surface wind speeds in hurricanes [17–19]. However, the retrieved results are mainly compared with the in situ surface wind speed observations below 30 m/s in [17–19]. They are not validated using the high wind measurements.

In this study, a new model for retrieving high wind speeds in hurricanes using WindSat C-band and X-band vertically and horizontally polarized brightness temperatures is proposed. The core of the new model is also based on the channel combination at different frequencies. Referring to [15], we define two new parameters, W6H and W6V, which represent an increment at 6H and 6V due to ocean wind, respectively. Finally, a wind speed retrieval algorithm for wind speeds above 20 m/s in hurricanes has been developed by using the two new parameters. The WindSat measurements for 15 category 4 and category 5 hurricanes from 2003 to 2010 and the corresponding H\*wind analysis data are used to develop and validate the retrieval model.

This paper is organized as follows. In Section 2, the datasets, including WindSat TBs, H\*wind analysis data, SFMR measurements, RSS global all-weather product and rain rate, are introduced. The methodology is presented in Section 3. Section 4 gives detailed results. The last section presents the conclusions.

## 2. Datasets

In this paper, WindSat TB measurements over hurricanes, and H\*wind analysis data are used to develop and test a new wind speed retrieval algorithm for inside hurricanes. The SFMR along-track wind speed measurements and the RSS global all-weather wind speed product are compared with the

retrieved wind speeds. In addition, the rain effect is also evaluated by using the RSS rain rate product. The selected datasets are described in the following sections.

### 2.1. Wind Sat Brightness Temperature

WindSat is a conically scanning passive microwave radiometer aboard the U.S. Department of Defense Coriolis satellite, which orbits the Earth in an 840-km circular sun-synchronous orbit. Its primary objective is to demonstrate the capability of a polarimetric microwave radiometer to measure the ocean surface wind vector from space. WindSat operates in 5 channels: 6.8, 10.7, 18.7, 23.8, and 37 GHz. All are fully polarimetric except for the 6.8 and 23.8 GHz channels, which feature dual polarization (vertical and horizontal). The integrated field of view (IFOV) is  $40 \times 60$  km,  $25 \times 38$  km,  $16 \times 27$  km,  $12 \times 20$  km, and  $8 \times 13$  km for the 6.8, 10.7, 18.7, 23.8, and 37 GHz channels, respectively. WindSat takes TB observations during both the forward-looking and the aft-looking scans. The forward-looking swath is approximately 1000 km and the aft-looking swath is approximately 400 km. During each scan, every channel is of a different location and resolution. Hence, the TB measurements must be resampled and averaged to a common size for wind vector retrieval. The selected TB measurements have been averaged to the 6.8 GHz footprint size with the WindSat ground data processing version 2.0 algorithm. A detailed description of the WindSat instrument can be found in [20]. In this paper, we only use the vertically and horizontally polarized measurements for wind speed retrieval.

### 2.2. H\*wind Products

Validation of hurricane surface wind fields is inherently challenging because there is no realizable “surface truth” data. Fortunately, a relatively reliable and reasonable estimation of tropical cyclone (TC) wind fields has been developed through the H\*wind analysis system. The wind fields produced by this system have been extensively used to study the wind speed retrieval algorithms under severe weather conditions [10,11,15,21–24]. H\*wind is a software tool that provides an objective analysis of the 1-min sustained-wind field at a height of 10 m above the sea surface and was developed by the Hurricane Research Division (HRD) of the Atlantic Oceanographic and Meteorological Laboratory [25]. The H\*wind analysis system assimilates all available surface observations, such as buoys, ships, C-MAN platforms, and surface airways, and all available aircraft and remote sensing data sources, which typically includes the SFMR, QuikSCAT, SSM/I, Geostationary Operational Environmental Satellite (GOES) low-level cloud drift winds, and Global Positioning System (GPS) dropwindsondes from aircraft. Typical wind speed errors in an H\*wind analysis are estimated to be 10% to 20% [26]. The wind speed errors in this analysis will vary depending on the quantity and quality of data that are available, as well as on the degree of quality control employed by the analyst. Although each wind speed analysis produced by this system may be inaccurate, the ensemble average over a large number of collocations can minimize the error in the overall analysis.

A hurricane is defined as storm with wind speeds exceeding 65 knots (33.5 m/s) [15]. The hurricanes selected for this paper are Fabian and Isabel in 2003; Frances and Ivan in 2004; Dennis, Katrina, Rita, and Wilma in 2005; Helene in 2006; Felix in 2007; Bertha and Ike in 2008; Bill and Ida in 2009; and Igor in 2010. The hurricane best track analysis and the corresponding intensity are depicted in Figure 1. These data can be obtained from the Automated Tropical Cyclone Forecast system [27], with products available at the National Oceanic Atmospheric Administration (NOAA) National Hurricane Center (NHC).

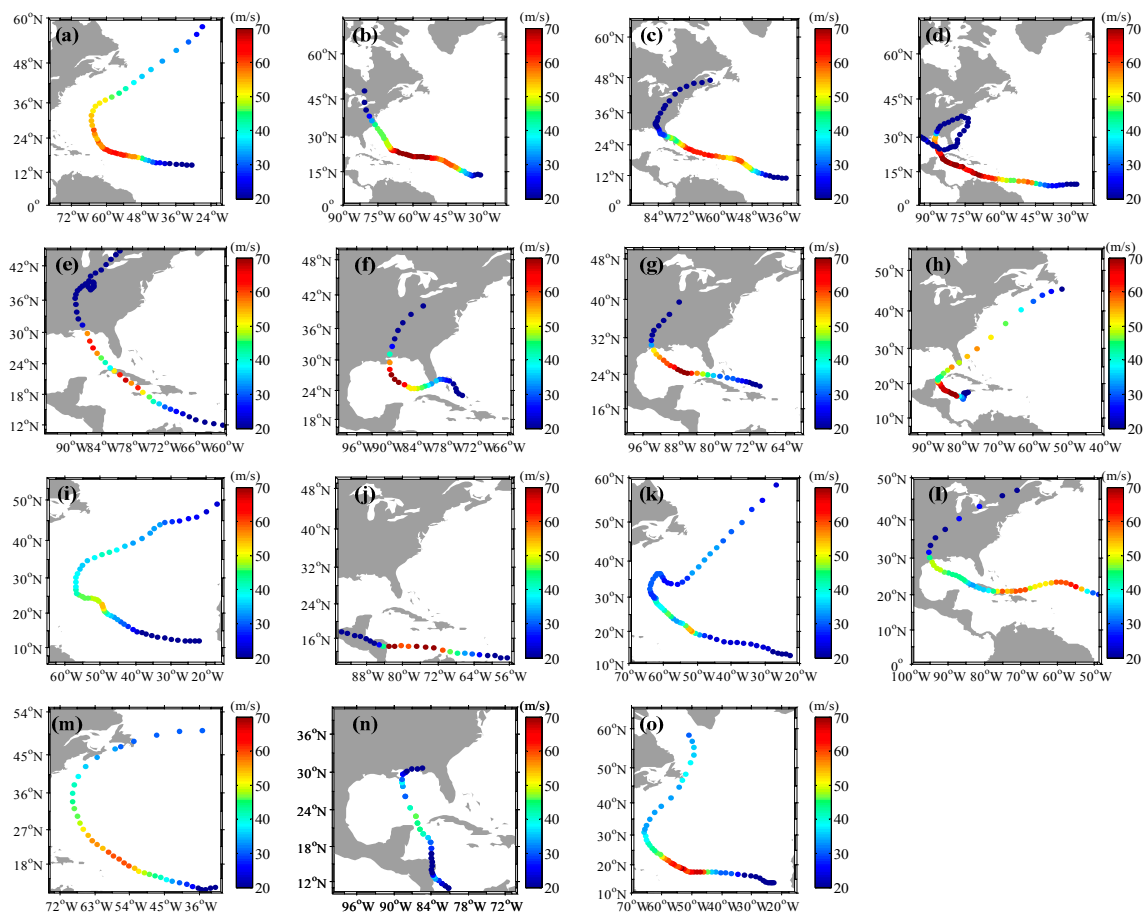


**Figure 1.** Best track positions and the corresponding intensity of the selected hurricanes for (a) Fabian, 27 August–9 September 2003; (b) Isabel, 6–19 September 2003; (c) Frances, 25 August–9 September, 2004; (d) Ivan, 2–24 September 2004; (e) Dennis, 4–17 July 2005; (f) Katrina, 23–30 August 2005; (g) Rita, 18–26 September 2005; (h) Wilma, 15–26 October 2005; (i) Helene, 12–26 September 2006; (j) Felix, 31 August–6 September 2007; (k) Bertha, 3–21 July 2008; (l) Ike, 1–15 September 2008; (m) Bill, 15–25 August 2009; (n) Ida, 4–11 November 2009; and (o) Igor, 8–22 September 2010.

### 2.3. Airborne Stepped-Frequency Microwave Radiometer (SFMR) Measurements

An SFMR is an airborne remote sensing instrument designed for retrieving surface wind speed and rainfall in TCs [28]. The first operational SFMR was flown on the WP-3D aircraft in 2004 [29]. An SFMR observes the nadir brightness temperatures at 6 C-band frequencies, i.e., 4.55, 5.06, 5.64, 6.34, 6.96, and 7.22 GHz. The TB measurements are processed with a 10-second running mean to retrieve ocean surface wind speed using a geophysical model function that relates the surface emissivity to wind speed. Global Positioning System dropwindsonde measurements have been used to validate the SFMR wind speed estimates, and the RMS error is approximately 4 m/s for measured wind speeds ranging from 10 to 70 m/s [29]. A previous study [30] shows that the SFMR wind speed in heavy precipitation has been further improved by using the new relationship between microwave absorption and rain rate. The advantage of SFMR is that it can potentially retrieve ocean surface wind speed at a relatively high spatial resolution (1.5 km). However, it can only provide point measurements along the aircraft flight track.

### 2.4. Other Sources

Using WindSat TB measurements, a global all-weather wind speed retrieval algorithm has been established by RSS [10]. It is a semi-statistical algorithm that can be applied in all rainy atmospheres

over the whole Earth. The estimated RMS accuracy of this algorithm ranges from approximately 2.0 m/s in light rain to approximately 5.0 m/s in heavy rain, if C-band channels and higher frequencies are available [10]. It is a good candidate for comparison with our retrieved wind speed results using WindSat TB measurements because the sufficient matchups can be obtained from them. We obtain the latest RSS v7.0.1 all-weather wind speed products from the RSS website (<http://www.remss.com/>).

To analyze the effect of rain, the RSS WindSat v7.0.1 rain rate product is used to directly study the wind speed retrieval errors. The other independent rain rate products are not selected because the time difference may result in a spatial mismatch [31]. For example, a TC with a forward motion of 10 m/s could travel 24 km in 40 min, comparable to the mean spatial resolution of the selected TB. In addition, the distribution of rainfall inside TCs is complex and changeable. To some extent, the mismatch could introduce some errors. We obtain the rain rate product from the RSS website (<http://www.remss.com/>), and the product was developed using the Unified Microwave Ocean Retrieval Algorithm (UMORA) [32].

### 2.5. Matchup

For training and testing the wind speed retrieval algorithm in TCs, we collected TB measurements over the H\*wind analysis fields. For WindSat, we collected data from 15 hurricanes during the period from 2003 to 2010. The time of the H\*wind analysis data and the average time of the WindSat overpass are within 3 h. No temporal interpolation is performed as the time intervals are too large in most cases. Within the 3-h time window between the products, the hurricane could have moved over a relatively large distance in some cases, which could introduce significant error. Thus, we shift the H\*wind analysis data for each TC based on the “best track” fixes from NHC so that the eye of the H\*wind analysis data coincides with the eye of the WindSat measurements. In addition, the H\*wind analysis fields are performed at a high resolution, which is approximately 5 km [25].

We resample the H\*wind analysis data to make them comparable to the low-resolution (6.9 GHz) WindSat TB measurements. Using a nearest neighbor interpolation, all H\*wind data points within a radius of 30 km (around the size of the WindSat 6.8 GHz IFOV) of the WindSat TB locations are weighted, inversely proportional to distance, and then averaged:

$$WS = \frac{\sum_{i=1}^n H^* \text{ wind } (i) \times \text{weight } (i)}{\sum_{i=1}^n \text{weight } (i)} \quad (1)$$

The function of weight is

$$\text{weight } (i) = \exp \left( \frac{-\text{dis } (i) \times \text{dis } (i)}{4 \times 30} \right) \quad (2)$$

where the “dis” is the distance (in kilometers) from an H\*wind point to a WindSat grid point. The form of weighting function is selected because it is based on the fact that the power that is received by the radiometer falls off roughly exponentially with distance and that wind speed is roughly proportional to the brightness temperature (power).

A previous study has shown that the radiometer TB is directly sensitive to surface roughness rather than wind speed [10]. The H\*wind analysis reports peak wind speeds for 1-min sustained winds. Thus, we need to convert from 1-min sustained H\*wind data to 10 min sustained satellite wind speeds because the surface winds for producing the surface roughness of the satellite measurements need to be sustained a longer time, which is at least 10 min. A derived scale factor of 0.88 is used here and by the U.S. Navy [33].

Table 1 lists the statistics of the selected TCs in the datasets, which includes the TC name, year, maximum wind speed, the latitudinal and longitudinal shifts of the TC eye, and the population of the selected wind speed above 20 m/s. Finally, the collocations contain 26,242 matchups for the WindSat.

**Table 1.** Statistics of matchups between WindSat observations and H\*wind analysis data for each selected TC.

	Year	Max Winds (m/s)	WindSat-H*wind		
			Population (ws > 20m/s)	Longitude Shift (°)	Latitude Shift (°)
Fabian	2003	60	1451	−0.054	−0.287
Isabel	2003	73	3633	−0.133	−0.058
Frances	2004	58	2390	−0.018	0.166
Ivan	2004	70	4012	−0.318	−0.264
Dennis	2005	65	1021	0.129	0.033
Katrina	2005	75	798	0.233	−0.050
Rita	2005	78	2673	0.362	−0.028
Wilma	2005	80	932	−0.169	−0.223
Helene	2006	53	1409	0.042	−0.050
Felix	2007	73	555	0.280	−0.132
Bertha	2008	53	1275	−0.135	−0.053
Ike	2008	63	2199	−0.006	−0.054
Bill	2009	58	376	−0.225	−0.346
Ida	2009	45	548	0.028	−0.077
Igor	2010	68	2970	−0.047	−0.033

### 3. Methodology

#### 3.1. Polarimetric Microwave Radiation

The Stokes parameters are a set of values that characterize the polarization state of the electromagnetic radiation. Four parameters,  $I$ ,  $Q$ ,  $U$ , and  $V$ , were defined by George Gabriel Stokes in 1852. Since passive microwave radiometers usually provide vertically and horizontally polarized brightness temperatures ( $T_V$  and  $T_H$ ) to observe the Earth, an alternate Stokes vector can be represented as  $T_V$ ,  $T_H$ ,  $T_3$ , and  $T_4$ :

$$TB = \begin{bmatrix} T_V \\ T_H \\ T_3 \\ T_4 \end{bmatrix} = c \times \begin{bmatrix} \langle |E_V|^2 \rangle \\ \langle |E_H|^2 \rangle \\ 2\text{Re} \langle E_V E_H^* \rangle \\ 2\text{Im} \langle E_V E_H^* \rangle \end{bmatrix} \quad (3)$$

where  $T_V$  and  $T_H$  describe the brightness temperatures of vertical and horizontal polarizations, respectively.  $T_3$  and  $T_4$  are the cross-correlation terms between these two orthogonal polarizations. In addition,  $c$  is a constant relating the brightness temperature to the electric energy density [34,35].

In recent years, various geophysical parameters, such as the wind vector, sea surface temperature, atmospheric water vapor, cloud liquid water, rain rate, and soil moisture, have been estimated by using the polarimetric brightness temperatures [8,9,36,37]. The brightness temperatures measured by the spaceborne polarimetric radiometer are the sum of the upwelling atmospheric radiation ( $T_{BU}$ ), the reflected cosmic background radiation ( $T_{BC}$ ) and the downwelling atmospheric radiation ( $T_{BD}$ ), and the emission of the ocean surface. The atmosphere attenuates the emission of the ocean surface and the reflected downwelling radiation. Thus, the four Stokes parameters received by a spaceborne polarimetric radiometer at each frequency can be expressed as follows [34]:

$$T_V = T_{BU} + \tau [e_v T_S + r_v (\Omega_v T_{BD} + \tau T_{BC})] \quad (4)$$

$$T_h = T_{BU} + \tau [e_h T_S + r_h (\Omega_h T_{BD} + \tau T_{BC})] \quad (5)$$

$$T_3 = \tau e_3 [T_S - (T_{BD} + \tau T_{BC})] \quad (6)$$

$$T_4 = \tau e_4 [T_S - (T_{BD} + \tau T_{BC})] \quad (7)$$

where  $e_p$  refers to the ocean surface emissivity at polarization  $p$  ( $p = v, h$ ), and the corresponding ocean surface reflectivity is  $r_p = 1 - e_p$ .  $T_S$  is the sea surface temperature, and  $\tau$  is the transmissivity of the atmosphere. The  $\Omega_p$  ( $p = v, h$ ) term is a correction factor to account for nonspecular reflection of the  $T_{BD}$  from the rough ocean surface [38]. Figure 2 describes the brightness temperatures received by a radiometer.

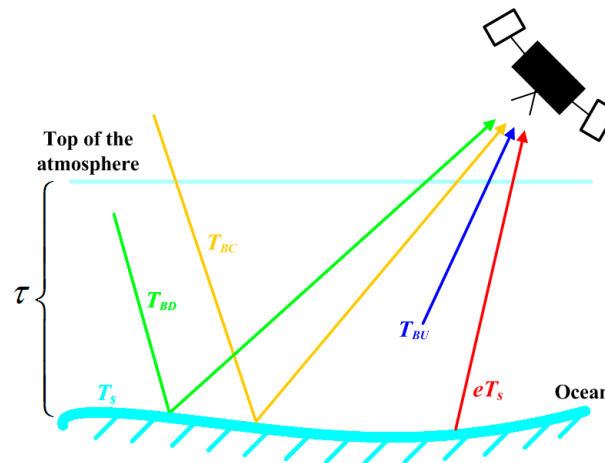
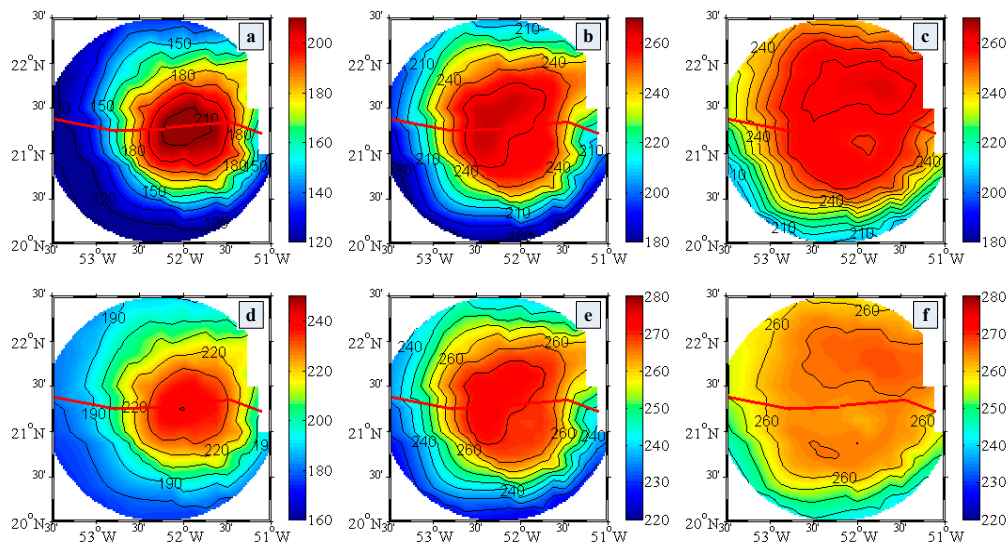


Figure 2. The brightness temperatures received by a radiometer.

### 3.2. Channel Selection

Under clear weather conditions, it is common to select higher frequencies such as 36 GHz rather than lower frequencies for retrieving the low to moderate ocean surface winds because the sensitivity to ocean surface wind at higher frequencies is better than that at lower frequencies [15,39]. However, the higher frequencies are almost invalid for retrieval of high winds in the severe weather conditions because the atmospheric opacity for higher frequencies exceeds that for lower frequencies. Figure 3 shows the WindSat brightness temperatures for hurricane Isabel on 10 September 2003, along with the best track (piecewise red curve) analysis from the NHC. The top three panels of Figure 3 show the results of horizontally polarized brightness temperature for the 10.7, 18.7, and 37 GHz channels, respectively. Note that we use a different color scale for the 10.7, 18.7, and 37 GHz images to highlight similar spatial features with high radiances, which are apparent signatures of rain. A rain band extending from the center to the northeast can be clearly found in these panels. The 18.7 and 37 GHz channels are nearly saturated close to the eye of the hurricane because of the influence of precipitation. However, the maximum value of the 10.7 GHz channel near the eye of the hurricane is approximately 210 K, which is fairly far from saturation. Similar characteristics can be found at lower frequency, such as 6.8 GHz. In addition, similar results can also be found in the vertically polarized brightness temperatures in the bottom panels of Figure 3. Therefore, we can use the lower frequencies, such as the 6.8 and 10.7 GHz channels, to develop an algorithm for retrieval of high winds under severe weather conditions.



**Figure 3.** Brightness temperatures measured by WindSat orbit #3510 on 10 September 2003, over hurricane Isabel (a) at 10.7 GHz, horizontal polarization; (b) at 18.7 GHz, horizontal polarization; (c) at 37.0 GHz, horizontal polarization; (d) at 10.7 GHz, vertical polarization; (e) at 18.7 GHz, vertical polarization and (f) at 37.0 GHz, vertical polarization. The red curve denotes the best track, which was obtained from the NHC.

### 3.3. Wind Speed Retrieval Model

Previous studies have shown that the sensitivity to the ocean wind at horizontal polarization is larger than that at vertical polarization [7,40]. The study of [15] only used 6.9 and 10.7 GHz horizontal polarization (hereafter, 6H and 10H) data from AMSR-E to retrieve wind speed inside hurricanes. However, we retain the 6.9 and 10.7 GHz vertical polarization (hereafter, 6V and 10V) data in addition to the horizontal polarization data in this study. We find that the vertical polarization data also shows the same characteristics as the horizontal polarization data described in [15]. In this study, we provide an improved algorithm for retrieving wind speed inside TCs by using 6V(H) and 10V(H) brightness temperatures. Based on the study [15], we also assess the wind-induced emissivity changes at both 6V(H) and 10V(H) because we retrieve wind speed by combining data from these channels.

Firstly, the brightness temperatures are simulated using Equations (4) and (5). Generally, three processes should be taken into account: absorption, emission, and scattering. The atmospheric absorption includes three components: water vapor, oxygen, and liquid water in the form of clouds or rain [7]. The above components also emit microwave energy according to the ambient temperature. Meanwhile, scattering must be taken into account unless the microwave wavelength is much larger than the size of the raindrops. Previous studies have shown that the raindrop-induced scattering can be neglected for frequencies below 10 GHz when the rain rate is less than 12 mm/h [15,41]. Scattering has been neglected in our simulation because the selected profiles are in almost clear weather conditions.

The 60-level ECMWF model outputs are used to simulate the brightness temperatures [42] and were generated by the ERA-40 assimilation system, which relies on the 3-dimensional variational scheme described in [43]. The sampled database gathers profiles corresponding to various ocean conditions, and the highest surface pressure is 1049 hPa. The wind speed ranges from 0.15 to 21.43 m/s, and the sea surface temperature ranges from 278.34 to 305.02 K. In addition, the water vapor ranges from 4 to 55.64 mm, and the liquid water ranges from 0 to 0.19 mm. The atmospheric transmittance at different channels is computed from the standard radiative transfer equations [39,44]. Likewise, the downwelling and upwelling atmospheric brightness temperatures are also calculated from the standard radiative transfer equations [39,44]. Note that the oxygen, water vapor, and cloud liquid water absorption coefficient use O2-MPM93 expression [45], H2O-PWR98 expression [46], and clw-MPM93

expression [45], respectively. In addition, the ocean surface emissivity and the reflectivity are calculated with the RTTOV radiative transfer model [47], and the correction factors are derived from RTTOV v11.3. The cosmic background radiation is approximately 2.7 K.

To account for wind speed in ocean emission, one parameter is defined as  $6(10)P^*$  ( $P = V, H$ ), which represents the difference between the WindSat  $6(10)P$  and calm ocean emission, corrected for atmospheric effects. This parameter represents the quantity of ocean microwave emission changed by ocean wind at  $6(10)P$ , which is defined by Equation (8).

$$6(10)P^* = \text{WindSat}_{6(10)P} - \text{Atmos}_{6(10)P} - \text{CalmOcean}_{6(10)P} \quad (8)$$

$$\text{CalmOcean}_{6(10)P} = \text{SST} \times (1 - r_p) \quad (9)$$

where the  $\text{WindSat}_{6(10)P}$  is the brightness temperature measurement for the  $6(10)$  GHz channel at  $P$ -polarization ( $P = V, H$ ) and  $\text{CalmOcean}_{6(10)P}$  is the ocean emission for  $6(10)$  GHz channel under calm ocean conditions. The SST used here is from ECMWF. In addition,  $\text{Atmos}_{6(10)P}$  is calculated by referring to [48].

Figure 4a,b illustrate the relationships between  $6(10)V^*$  and ECMWF wind speed. The  $6(10)V^*$  decreases initially because the shielding effect has been found in the calculation of ocean emissivity at  $V$ -polarization and then increases with increasing wind speed. The sensitivity of  $6(10)V^*$  to wind speed is approximately  $0.37(0.5)$  K/(m/s) when the wind speed is from 8 to 20 m/s. Figure 4d,e show the relationships between  $6(10)H^*$  and ECMWF wind speed. The  $6(10)H^*$  increases with increasing wind speed, which is different from  $6(10)V^*$ . The sensitivity of  $6(10)H^*$  to wind speed is better than that of  $6(10)V^*$ , and it is approximately  $0.85(0.93)$  K/(m/s). The previous study [15] showed that the sensitivity of  $6H^*$  to wind speed is approximately  $1$  K/(m/s), which is higher than our calculated result. The diverse data resources may result in this difference. On the contrary, our calculated result of  $6H^*$  is higher than the experimental result [49], which indicates that the sensitivity at approximately  $6-7H$  is approximately  $0.5$  K/(m/s), even though the experiments are limited to ground-based observations. Figure 4c illustrate the relationships between the  $6V^*$  and  $10V^*$ . When the wind speed is from 0 to 20 m/s, the ratio of  $6V^*$  to  $10V^*$  is a constant which is approximately 0.82. The ratio of  $6H^*$  and  $10H^*$  has similar characteristics (Figure 4f), and the value is approximately 0.92. These results are in good agreement with the previous results [15,28].

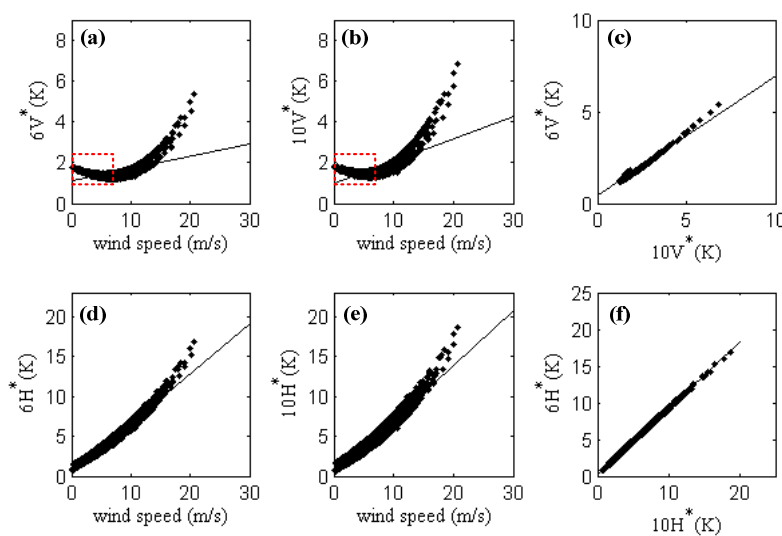


**Figure 4.** (a) Relationship between  $6V^*$  and ECMWF wind speed; (b) Relationship between  $10V^*$  and ECMWF wind speed; (c) Relationship between  $6V^*$  and  $10V^*$ ; (d) Relationship between  $6H^*$  and ECMWF wind speed; (e) Relationship between  $10H^*$  and ECMWF wind speed; (f) Relationship between  $6H^*$  and  $10H^*$ .

Making use of the fact that the ratio between  $6H^*$  and  $10H^*$  is a constant, Shibata [15] established a wind speed retrieval algorithm by assuming that this ratio still holds at higher wind speeds and under rainy conditions. Based on the Shibata method and the above discussions, we develop an improved algorithm with two new parameters known as W6V and W6H. The definitions of W6V and W6H are similar to the previous study [15]:

$$\begin{aligned} W6H &= EF^*/fac_1 = (6H^- - 6H_E^-)/fac_1 \\ &= (6H^- - c_1 \times 10H^- + a_1 \times c_1 - b_1) \times sl_1 / (sl_1 - c_1) / fac_1 \end{aligned} \quad (10)$$

$$sl_1 = d_1 + e_1 \times (10H_E^- - a_1) \quad (11)$$

$$fac_1 = 1 - f_1 \times (10H_E^- - a_1) \quad (12)$$

$$6(10)H^- = WindSat\_6(10)H - CalmOcean\_6(10)H \quad (13)$$

$$\begin{aligned} W6V &= EF^*/fac_2 = (6V^- - 6V_E^-)/fac_2 \\ &= (6V^- - c_2 \times 10V^- + a_2 \times c_2 - b_2) \times sl_2 / (sl_2 - c_2) / fac_2 \end{aligned} \quad (14)$$

$$sl_2 = d_2 + e_2 \times (10V_E^- - a_2) \quad (15)$$

$$fac_2 = 1 - f_2 \times (10V_E^- - a_2) \quad (16)$$

$$6(10)V^- = WindSat\_6(10)V - CalmOcean\_6(10)V \quad (17)$$

where the WindSat\_6(10)P and CalmOcean\_6(10)P are the same as Equations (8) and (9). The definition of other parameters in Equations (10) to (13) can be found in Figure 5. The brightness temperatures of group A (Figure 5a) are the results under calm ocean conditions. The brightness temperatures of group B (Figure 5a) are the results under rough ocean conditions. In Figure 5a, the relationship between 6H and 10H is slightly nonlinear, but we have approximated it as linear for simplicity. By calculating  $6(10)H^-$ , we can obtain Figure 5b, in which line A is approximated as a linear line passing through the point  $O(a_1, b_1)$  with the slope  $c_1$ . Point F in Figure 5b corresponds to an arbitrary point on line B in Figure 5a. Then, we can obtain an intersecting point E made by two lines OP and EF in Figure 5b. The slope of the line EF is  $sl_1$ . Finally, we can obtain the parameter “W6H” (unit: Kelvin) based on the length of  $EF^*$  divided by the atmospheric effect ( $=fac_1$ ). A detailed description can be found in [15]. The parameters for V-polarization in Equations (14) to (17) are similar to those of H-polarization in Equations (10) to (13).

Finally, we propose a new algorithm that relates W6V and W6H to wind speed (m/s):

$$\begin{aligned} WS &= 0.2034 \times W6H + 0.01 \times W6V + 15.3 && \text{if } W6H < 20 \\ WS &= 0.3017 \times (W6H - 20) + 0.2 \times (W6V - 30) + 22.65 && \text{if } 20 \leq W6H < 30 \\ WS &= 0.3 \times (W6H - 30) + 0.4 \times (W6V - 40) + 32.54 && \text{if } W6H \geq 30 \end{aligned} \quad (18)$$

The coefficients  $a_1 \sim f_1$  and  $a_2 \sim f_2$  in Equations (10) to (17) are listed in Table 2.

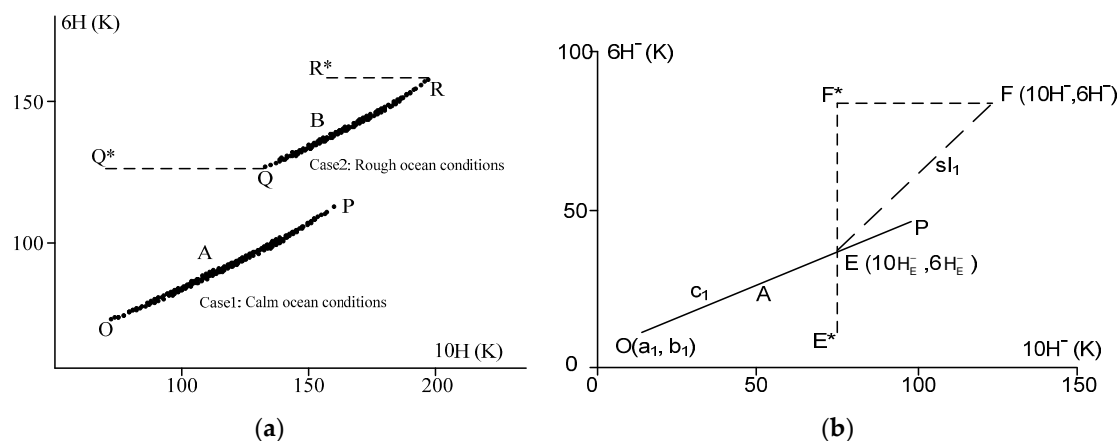


**Figure 5.** (a) Brightness temperatures of 6H and 10H: group A for calm ocean conditions and group B for rough ocean conditions; (b) Thematic figure drawn from (a). The two figures can be found in [15].

**Table 2.** Model coefficients in Equations (10) to (17).

$a_1$	$b_1$	$c_1$	$d_1$	$e_1$	$f_1$
14.1718	6.0173	0.3284	0.9521	0.0100	0.0010
$a_2$	$b_2$	$c_2$	$d_2$	$e_2$	$f_2$
17.0839	3.1643	0.4330	0.9529	0.0011	0.0018

## 4. Results

### 4.1. Brightness Temperature 6(10) $P^-$ Comparisons

Before calculating the fitted coefficients of the model, we must estimate the 6(10)  $P^-$  ( $P = V, H$ ) with Equation (13) and Equation (17). We first need to calculate the ocean TBs under the calm sea conditions, which are a function of frequency, polarization, incidence angle, SST and salinity. The SST derived from the Reynolds weekly analysis was used to estimate the ocean microwave emission at 6(10) GHz under the calm sea conditions with the Klein and Swift model [50]. For the salinity effect, the previous study [15] demonstrated that the sensitivity of TBs at 6.8 GHz H-polarization is 0.003 K/PSU at 0 °C SST and  $-0.039$  K/PSU at 30 °C SST for a salinity range of 30 to 35 PSU. The values for 10.7 GHz H-polarization are 0.006 K/PSU and  $-0.012$  K/PSU, respectively. Thus, the salinity effect is also negligible in our study.

Figure 6 shows the brightness temperatures of 6 $H^-$  ( $V^-$ ) and 10 $H^-$  ( $V^-$ ) inside and around hurricanes. The cases in which the center of the hurricane contains land areas were removed because 6 $H^-$  ( $V^-$ ) and 10 $H^-$  ( $V^-$ ) cannot be evaluated over land. Figure 6a shows the WindSat 6 $H^-$  and 10 $H^-$  from hurricane Fabian on 3 September 2003, and the maximum wind speed is 47 m/s. Figure 6b displays the WindSat 6 $H^-$  and 10 $H^-$  on 31 August 2004, with a maximum wind speed of 51 m/s for hurricane Frances. Figure 6c presents the WindSat 6 $H^-$  and 10 $H^-$  on 9 July 2005, with a maximum wind speed of 51 m/s for hurricane Dennis; Figure 6d–f illustrate the results of the vertically polarized channels. In Figure 6a, the data marked by arrow A correspond to the outer area around Fabian, and the data marked by B correspond to the area inside Fabian. The situation is similar for the other cases. In addition, the arrow B moves upward as the wind speed increases, and the above results are in good agreement with the previous study [15].

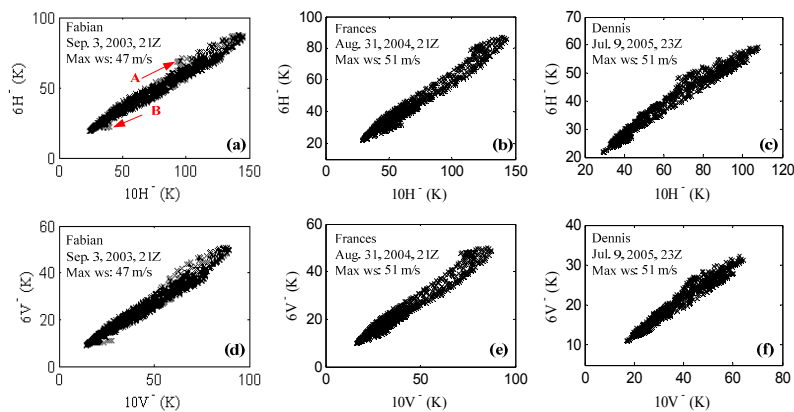


**Figure 6.** Relationships of WindSat  $6H^-$  and  $10H^-$  for three hurricanes: (a) Fabian (2003); (b) Frances (2004); and (c) Dennis (2005). Relationships of WindSat  $6V^-$  and  $10V^-$  for three hurricanes: (d) Fabian (2003); (e) Frances (2004); and (f) Dennis (2005).

#### 4.2. Wind Speed Retrieval and Validation

The new model is established by using 4862 matchups between WindSat TBs and H\*wind analysis data for Fabian (2003), Frances (2004), and Dennis (2005). We have checked that other groups of hurricanes give similar fitted coefficients for wind speed retrieval. The results show that the mean bias and RMS difference of the new model (Figure 7a) are 0.07 m/s and 2.63 m/s, respectively. Furthermore, we also compare the new model to the model of Shibata (2006) model with the old coefficients [15] and the new coefficients derived from our matchups, respectively. The performance of the new model is improved. The mean bias and RMS difference of the Shibata method with the new coefficients (Figure 7b) are  $-0.22$  m/s and 2.81 m/s, respectively, which are better than those retrieved with the Shibata model using the old coefficients that were derived from the simulations (with mean bias and RMS difference of 1.23 m/s and 5.13 m/s, respectively). In addition, the error increases with increasing wind speed for both the new model and the Shibata model. Through the above discussion, we can conclude the added V-polarization channels contribute to improving the retrieval performance.

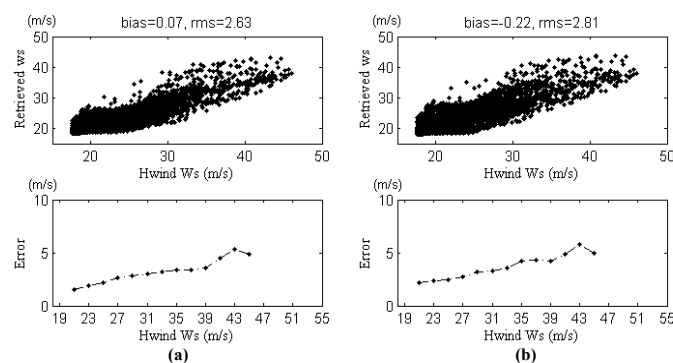


**Figure 7.** Retrieved wind speed of three hurricanes using our new method and the Shibata method with the new coefficients versus H\*wind analysis data. (a) Our new method and (b) the method of Shibata (2006) with the new coefficients.

##### 4.2.1. Comparison with H\*wind Analysis Data

Figure 8 presents the retrieved wind speed using the new model versus the corresponding H\*wind analysis data for each selected hurricane. The mean bias and RMS error are given in the top of each single panel. For wind speeds above 20 m/s, the mean bias and overall RMS difference of the new model are 0.04 m/s and 2.75 m/s, respectively, for 15 hurricanes from 2003 to 2010. Positive biases are found in some hurricanes, including Dennis, Katrina, Rita, Wilma, Helene, Ike, Bill, and Ida.

For hurricane Bill, in particular, the new model largely overestimates wind speeds, with a mean bias of 2.89 m/s. On the contrary, the largest negative bias ( $-1.45$  m/s) is found in hurricane Bertha. On the whole, the retrieved results have a good agreement with the H\*wind analysis wind speed.

It is challenging to retrieve wind speeds under severe weather conditions, especially in typhoons and hurricanes. Rain not only increases the atmospheric attenuation but also changes the sea surface roughness in a complicated manner. Thus, it is difficult to accurately model brightness temperatures under rainy conditions. Hence, the statistical algorithm is a relatively good candidate that can be used to retrieve wind speed under severe weather conditions. In general, the new wind speed retrieval algorithm under rain gives an encouraging accuracy compared to the H\*wind wind speed.

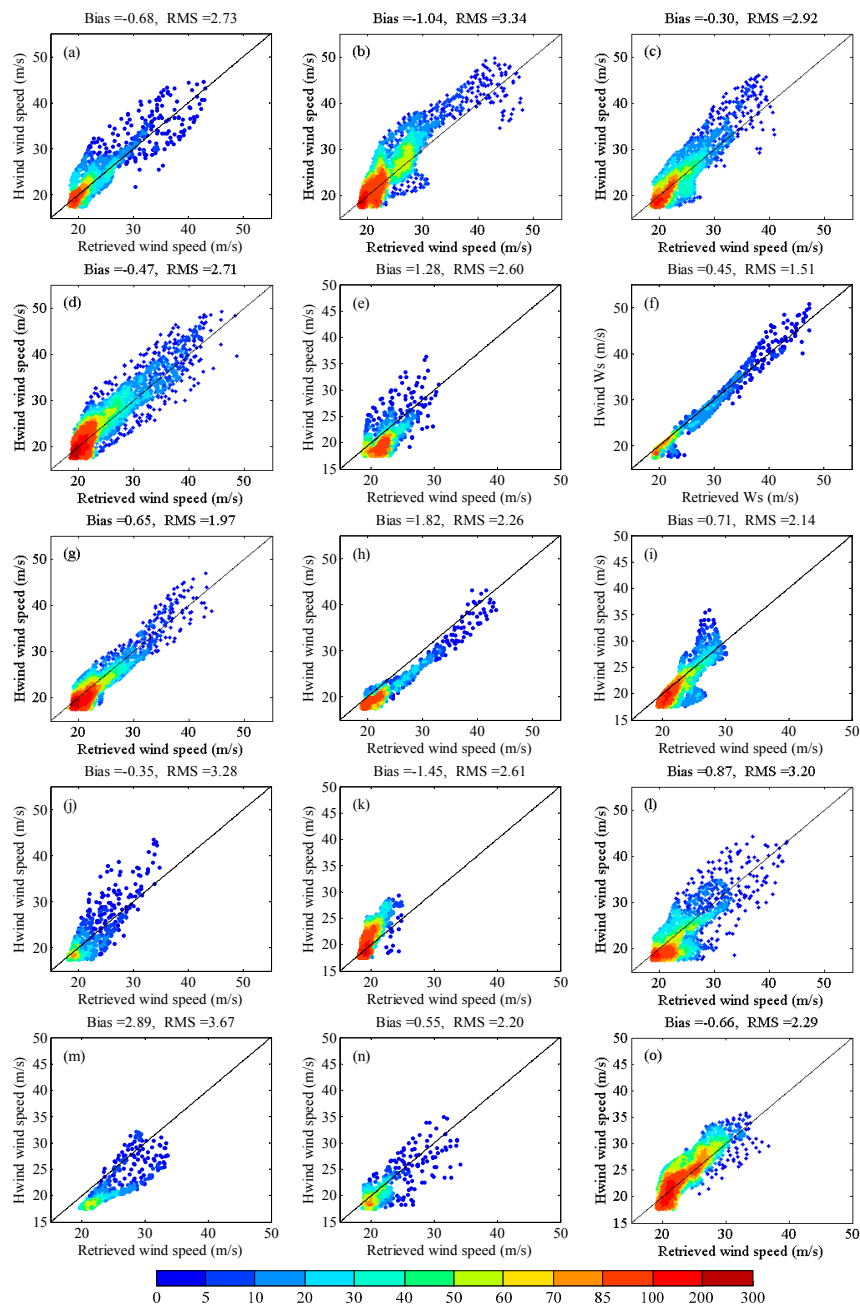


**Figure 8.** The comparisons between H\*wind wind speed and the retrieved wind speed with our new model using WindSat 6 and 10 GHz brightness temperatures for each selected hurricane: (a) Fabian; (b) Isabel; (c) Frances; (d) Ivan; (e) Dennis; (f) Katrina; (g) Rita; (h) Wilma; (i) Helene; (j) Felix; (k) Bertha; (l) Ike; (m) Bill; (n) Ida; and (o) Igor.

#### 4.2.2. Comparison with Remote Sensing Systems (RSS) All-Weather Data

A global all-weather wind speed product has been developed using the WindSat TBs [10], which is a good candidate for comparison to our retrieved wind speed results based on WindSat TBs inside hurricanes. Table 3 illustrates the retrieved wind speed using our new algorithm and the RSS global algorithm, respectively. The overall RMS difference of wind speed between our new model and H\*wind analysis data is lower than that between the RSS wind speed and H\*wind analysis data. In addition, results are similar for each individual case except for hurricane Bill. All biases are negative between the RSS wind speed and H\*wind analysis data. That means the RSS wind speed underestimates wind speed on the whole, especially for high wind speeds. The mean bias is  $-2.53$  m/s between them. Compared to the H\*wind analysis data, the retrieved wind speed using the new method overestimates wind speed slightly, and the mean bias is  $0.04$  m/s for the selected 15 hurricanes.

**Table 3.** Statistics of errors between the new retrieved wind speed and H\*wind wind speed and between RSS all-weather wind speed and H\*wind wind speed for H\*wind wind speeds above 20 m/s for the selected hurricanes from 2003 to 2010.

Hurricane Name	Ours		RSS	
	Bias (m/s)	RMS (m/s)	Bias (m/s)	RMS (m/s)
Fabian	-0.68	2.73	-3.02	4.26
Isabel	-1.04	3.34	-3.25	4.39
Frances	-0.30	2.92	-3.03	4.66
Ivan	-0.47	2.71	-2.68	3.65
Dennis	1.28	2.60	-2.46	3.89
Katrina	0.45	1.51	-2.32	3.68
Rita	0.65	1.97	-2.38	3.20
Wilma	1.82	2.26	-1.65	2.90
Helene	0.71	2.14	-1.86	3.25
Felix	-0.35	3.28	-2.80	4.21
Bertha	-1.45	2.61	-4.30	5.40
Ike	0.87	3.20	-2.30	4.04
Bill	2.89	3.67	-1.40	3.25
Ida	0.55	2.20	-1.50	4.00
Igor	-0.66	2.29	-1.73	3.29
All together	0.04	2.75	-2.53	3.91

#### 4.2.3. Comparison with SFMR Measurements

The SFMR measurements are compared with our retrieved wind speed results, although these data can only provide point observations along the aircraft flight track. The 30-min window is utilized to collocate the matchups between the WindSat data and SFMR measurements. Since the SFMR measurements are at a high spatial resolution of 1.5 km, a method similar to that described in section 2.5 is also performed. Finally, we obtained 938 wind speed matchups for the selected 15 hurricanes. Figure 9 suggests that the derived wind speed has a relatively good agreement with the SFMR measurements, with a mean bias of  $-0.68$  m/s and an RMS difference of 3.14 m/s. The general trend is that the retrieved wind speed errors increase with increasing SFMR rain rate.

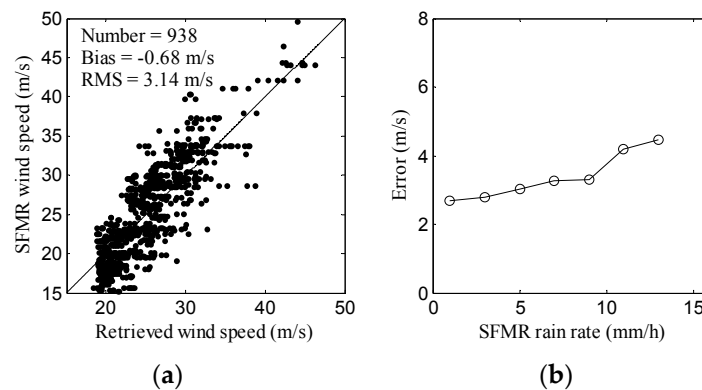


**Figure 9.** (a) The comparison between SFMR wind speeds and the retrieved wind speeds with our new method; (b) Errors of the retrieved wind speeds versus SFMR rain rate.

#### 4.3. Case Studies

As a case study (denoted as Rita-1), two different models are used to retrieve wind speed using the WindSat TBs for hurricane Rita on 22 September 2005, at 1330 UTC. Figure 10a presents the H\*wind analysis wind speed, and Figure 10b shows the retrieved wind speed using our new model. Figure 10c shows the retrieved wind speed using the RSS global algorithm, and Figure 10d illustrates the corresponding RSS rain rate. Figure 10e shows the difference between the retrieved wind speed and the H\*wind analysis data. The difference between the RSS wind speed and the H\*wind analysis data is presented in Figure 10f. In addition, the corresponding W6H and W6V are presented in Figure 10g,h, respectively. In this case, the H\*wind analysis wind speed is obtained for 22 September 2005, at 1330 UTC. At that time, the center of typhoon's eye was located at 25.197°N and -88.531°E. However, the center of typhoon's eye was located at 25.141°N and -88.237°E at the time of the WindSat observation, which is obtained from the NHC. Therefore, we shifted the H\*wind analysis wind speed so that the eye of the H\*wind analysis coincides with eye of the WindSat measurement. Comparing W6H with W6V, we find that W6H seems to have a better correlation than W6V. The distribution of W6H is similar to that of wind speed. The performance of the new model is satisfied, and the distribution of retrieved wind speed is very close to the H\*wind analysis wind speed, with the mean bias of 0.79 m/s and RMS difference of 1.79 m/s. As for RSS wind speeds, the influence of rain is obvious. On the contrary, our new model can reduce the influence of rain to some extent, and the retrieved results (Figure 10e) are in good agreement with the H\*wind analysis wind speed. In general, the RSS global wind speed underestimates the wind speed in most regions, and the retrieved results are vulnerable to rain (Figure 10f). In addition, it is seen that the retrieved wind speed overestimates wind speed in the center of the eye for our retrieved results and RSS wind speeds. This may be because there are still strong waves that increase the emission from ocean surface, even though the wind speed is relatively low in the eye of the typhoon.

In a second case study (denoted as Rita-2), the two different models are also utilized to retrieve wind speed with the WindSat TBs for hurricane Rita on 22 September 2005, at 0130 UTC. Figure 11b illustrates the retrieved wind speed using our new model. Figure 11c shows the retrieved wind speed using the RSS global algorithm, and Figure 11d shows the corresponding RSS rain rate. Figure 11e–f present the difference between the retrieved wind speeds and the H\*wind analysis data. In addition, Figure 11g,h show the corresponding W6H and W6V results, respectively. In this case, the center of the typhoon's eye is located at 24.536°N and -87.238°E for the H\*wind analysis data; however, the center of typhoon's eye is located at 24.535°N and -86.808°E at the time of the WindSat observation. Hence, we shifted the H\*wind analysis wind speed so that the eye of the H\*wind analysis wind speed coincides with eye of the WindSat measurement. The results show that the performance of the new model is satisfied, and the mean bias and RMS difference of the new model are 0.63 m/s and 2.38 m/s,

respectively. Near the south of the typhoon's eye, our new model seems to underestimate wind speed when the rain rate is relatively low, and similar results are also found in the RSS global algorithm.

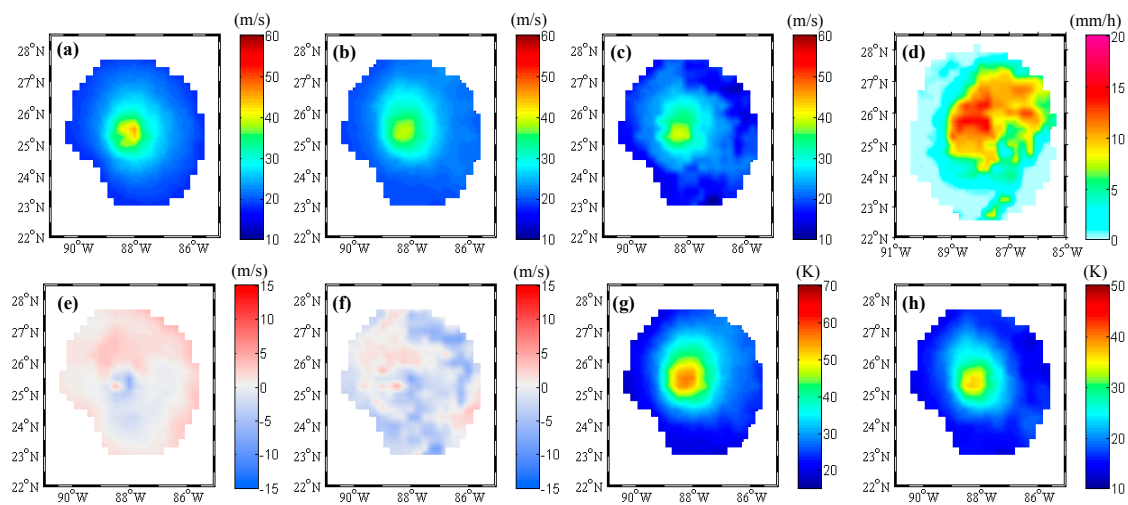


**Figure 10.** (a) H\*wind wind speed of Rita on 22 September 2005, at 1330 UTC; (b) Retrieved wind speed of Rita with our new model on 22 September 2005, at 1155 UTC; (c) RSS all-weather wind speed of Rita on 22 September 2005, at 1155 UTC; (d) RSS rain rate of Rita on 22 September 2005, at 1155 UTC; (e) The bias between H\*wind and Retrieved wind speed with our new model; (f) The bias between H\*wind and RSS all-weather wind speed; (g) W6H over Rita on 22 September 2005, at 1155 UTC; (h) W6V over Rita on 22 September 2005, at 1155 UTC.

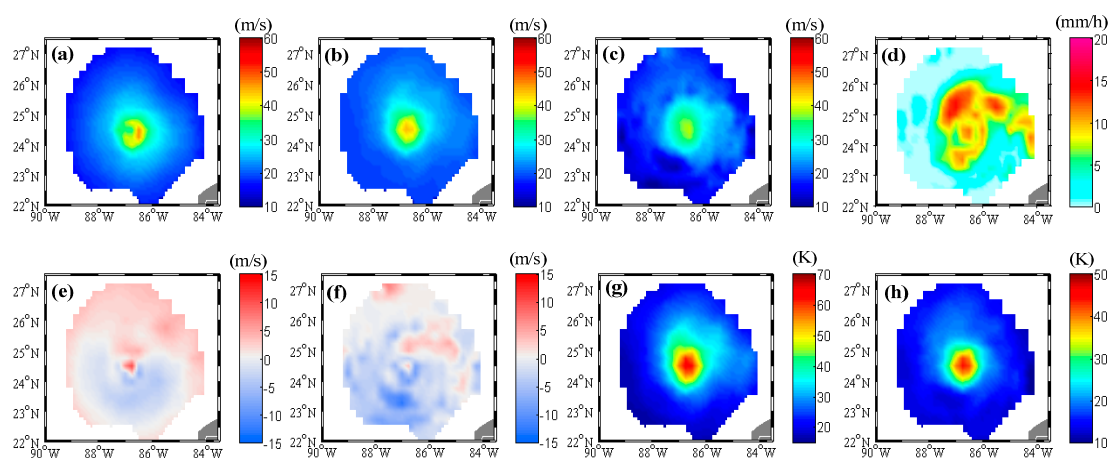


**Figure 11.** (a) H\*wind wind speed for Rita on 22 September 2005, at 0130 UTC; (b) Retrieved wind speed based on our new model for Rita on 21 September 2005, at 2328 UTC; (c) RSS all-weather wind speed for Rita on 21 September 2005, at 2328 UTC; (d) RSS rain rate for Rita on 21 September 2005, at 2328 UTC; (e) The bias between H\*wind and the wind speed retrieved with our new model; (f) The bias between H\*wind and the RSS all-weather wind speed; (g) W6H over Rita on 21 September 2005, at 2328 UTC; (h) W6V over Rita on 21 September 2005, at 2328 UTC.

#### 4.4. Rain Effects on Wind Retrieval

The passive radiometer measurement is less sensitive to the ocean surface wind speed under rainy conditions. Rain increases the atmospheric attenuation, which is obvious at higher frequencies (Figure 3). In addition, it is very difficult to accurately simulate the brightness temperatures in rain, especially for the high variability of rainy atmospheres. The brightness temperatures depend on cloud type and the distribution of rain within the footprint [32,51]. Then, the full Mie absorption theory

needs to be applied to calculate the atmospheric radiative transfer equation, which requires additional input parameters, such as size and form of the rain drops; however, these parameters are not readily available. Therefore, previous studies have mainly focused on the statistical algorithm for retrieving wind speed under rainy conditions [10,15,17].

Using the RSS rain rate products, the rain effect is evaluated in the new model. Table 4 presents the biases and RMS errors of the difference between the wind speeds from the retrievals and the corresponding H\*wind analysis wind speeds as a function of the WindSat rain rate. In general, the biases are negative when the rain rate is less than 4 mm/h or more than 14 mm/h. Therefore, the retrieved wind speed underestimates wind speed in this situation. The biases become positive when the rain rate ranges from 4 to 14 mm/h. In general, the wind speed retrieval errors increase with increasing rain rate. The wind speed retrieval accuracy of our new model inside hurricane ranges from 2.0 m/s in light rain to 3.9 m/s in heavy rain.

**Table 4.** The statistics for different rain intervals between H\*wind wind speed and the wind speed retrieved with our new method.

Rain Interval (mm/h)	Average Rain Rate (mm/h)	Number	Bias (m/s)	RMS (m/s)
[0, 2]	0.55	10495	−0.37	1.96
[2, 4]	3.02	3241	−0.11	2.52
[4, 6]	5.03	3532	0.18	2.72
[6, 8]	7.00	2920	0.57	2.85
[8, 10]	9.06	2633	0.33	3.15
[10, 12]	10.95	1869	0.73	3.59
[12, 14]	12.86	1044	0.49	3.73
above 14	14.73	508	−0.57	3.89

## 5. Conclusions

In this study, we assess the wind-induced emissivity changes in C-band and X-band channels using simulated brightness temperatures. Four parameters ( $6V^*$ ,  $6H^*$ ,  $10V^*$ , and  $10H^*$ ) are defined, and they present the quantity of ocean microwave emission changed by ocean wind. The results show that the sensitivity of  $6(10)V^*$  to wind speed is approximately  $0.37(0.5)$  K/(m/s) and that the sensitivity of  $6(10)H^*$  to wind speed is approximately  $0.85(0.93)$  K/(m/s). Furthermore, we find that the ratio of  $6V(H)^*$  to  $10V(H)^*$  is a constant, which is approximately  $0.82(0.92)$ . These results are in good agreement with previous studies [15,28]. Based on the work in [15], we define two new parameters,  $W6H$  and  $W6V$ , which represent increments in  $6H$  and  $6V$  due to ocean wind, respectively. Finally, a wind speed retrieval algorithm for wind speeds above 20 m/s in hurricanes has been developed using the two new parameters. The C-band and X-band vertically and horizontally polarized brightness temperatures are used to retrieve high wind speeds because the brightness temperature acquired at higher frequencies become saturated inside hurricanes.

The WindSat measurements over 15 hurricanes from 2003 to 2010 and the corresponding H\*wind analysis data are used to develop and validate the retrieval model. The performance is encouraging, with a mean bias of 0.04 m/s and an overall RMS difference of 2.75 m/s. In general, the retrieved wind speeds have a good agreement with the H\*wind analysis wind speeds. Two case studies are performed, resulting in a mean bias and RMS difference of 0.79 m/s and 1.79 m/s for hurricane Rita-1 and 0.63 m/s and 2.38 m/s for hurricane Rita-2. Compared to the RSS global all-weather wind speeds, our retrieved wind speeds is closer to the H\*wind analysis data, and the RSS global all-weather wind speeds underestimates the wind speed. In addition, the retrieved wind speeds are compared to the SFMR wind speeds. Good agreement is found between them.

It is a challenging job to retrieve wind speed under rainy conditions, especially for typhoons and hurricanes. The core of the new algorithm for determining the wind speed under rainy conditions involves using different channel combinations that reduce the signal coming from rain without greatly

reducing the wind speed signal. With respect to the effect of rain, the performance of the new model inside hurricanes ranges from 2.0 m/s in light rain to 3.9 m/s in heavy rain. The performance of retrieving wind speed under rainy conditions is satisfactory.

This new algorithm can be used to retrieve wind speeds in hurricanes under rainy conditions with an encouraging degree of accuracy, although we cannot expect the algorithm to have the same accuracy as in rain-free cases. It is noted that the retrieved wind speed always overestimates wind speed in the eye of the hurricane. That may be because there are still strong waves that increase the emission from the ocean surface, even if the wind speed is relatively low in the eye of hurricane. For practical applications of the new wind speed algorithm, we should update the current method for hurricanes in which the areas of high wind and high rain are not fully observed. In addition, the relationship between wind speed and wind-induced emissivity under different sea states, wave ages, and air-sea stability in hurricanes should be studied. Furthermore, the wind direction retrieval will be studied using the polarimetric brightness temperatures in the future.

**Acknowledgments:** This work was funded by the National Natural Science Foundation of China (Grant Nos. 61501433; 41576171). This work was also supported by CAS frontier science key research projects (Grant No. QYZDB-SSW-SYS010). We thank the Computational Physics. Inc. for providing WindSat brightness temperature and the Hwind Corporate Office for providing the H\*wind analysis data. WindSat global all-weather wind product and rain rates are produced by Remote Sensing Systems and sponsored by the NASA Earth Science MEASUREs DISCOVER Project and the NASA Earth Science Physical Oceanography Program. SFMR data are provided by the Hurricane Research Division, NOAA.

**Author Contributions:** L.Z. and X.Y. originated the main concept of this study. L.Z. carried out the experiments, analysis and writing in this study; X.Y. provided some constructive suggestions and revised the manuscript; H.S. and Z.W. contributed to the discussion of the results.

**Conflicts of Interest:** The authors declare no conflict of interest.

## References

1. Gentemann, C.L.; Wentz, F.J.; Brewer, M.; Hilburn, K.; Smith, D. Passive microwave remote sensing of the ocean: An overview. In *Oceanography from Space*; Barale, V., Gower, J.F.R., Alberotanza, L., Eds.; Springer: Hague, The Netherlands, 2010; pp. 13–33.
2. Hollinger, J.P.; Peirce, J.L.; Poe, G.A. SSM/I instrument evaluation. *IEEE Trans. Geosci. Remote Sens.* **1990**, *28*, 781–790. [[CrossRef](#)]
3. Goodberlet, M.A.; Swift, C.T.; Wilkerson, J.C. Ocean surface wind speed measurements of the Special Sensor Microwave/Imager (SSM/I). *IEEE Trans. Geosci. Remote Sens.* **1990**, *28*, 823–828. [[CrossRef](#)]
4. Atlas, R.; Hoffman, R.N.; Bloom, S.C.; Jusem, J.C.; Ardizzone, J. A multiyear global surface wind velocity dataset using SSM/I wind observations. *Bull. Am. Meteorol. Soc.* **1996**, *77*, 869–882. [[CrossRef](#)]
5. Yu, L.; Jin, X. Buoy perspective of a high-resolution global ocean vector wind analysis constructed from passive radiometers and active scatterometers (1987–present). *J. Geophys. Res.* **2012**. [[CrossRef](#)]
6. Wentz, F.J. Measurement of oceanic wind vector using satellite microwave radiometers. *IEEE Trans. Geosci. Remote Sens.* **1992**, *30*, 960–972. [[CrossRef](#)]
7. Wentz, F.J.; Meissner, T. *AMSR Ocean Algorithm, Algorithm Theoretical Basis Document*; RSS Technical Report 121599A-1; Remote Sensing Systems: Santa Rosa, CA, USA, 2000.
8. Meissner, T.; Wentz, F.J. Ocean retrievals for WindSat: Radiative transfer model, algorithm, validation. In Proceedings of the 9th Specialist Meeting on Microwave Radiometry and Remote Sensing, San Juan, PR, USA, 28 February–3 March 2006; pp. 4761–4764.
9. Bettenhausen, M.H.; Smith, C.K.; Bevilacqua, R.M.; Wang, N.Y.; Gaiser, P.W.; Cox, S. A nonlinear optimization algorithm for WindSat wind vector retrievals. *IEEE Trans. Geosci. Remote Sens.* **2006**, *44*, 597–610. [[CrossRef](#)]
10. Meissner, T.; Wentz, F.J. Wind-vector retrievals under rain with passive satellite microwave radiometers. *IEEE Trans. Geosci. Remote Sens.* **2009**, *47*, 3065–3083. [[CrossRef](#)]
11. Neul, N.; Tenerelli, J.; Chapron, B.; Vandemark, D.; Quilfen, Y.; Kerr, Y. SMOS satellite L-band radiometer: A new capability for ocean surface remote sensing in hurricanes. *J. Geophys. Res.* **2012**. [[CrossRef](#)]
12. Yueh, S.H. Directional signals in Windsat observations of hurricane ocean winds. *IEEE Trans. Geosci. Remote Sens.* **2008**, *46*, 130–136. [[CrossRef](#)]

13. Yan, B.; Weng, F. Applications of AMSR-E measurements for tropical cyclone predictions part I: Retrieval of sea surface temperature and wind speed. *Adv. Atmos. Sci.* **2008**, *25*, 227–245. [[CrossRef](#)]
14. Mai, M.; Zhang, B.; Li, X.F.; Hwang, P.A.; Zhang, J.A. Application of AMSR-E and AMSR2 Low-Frequency Channel Brightness Temperature Data for Hurricane Wind Retrievals. *IEEE Trans. Geosci. Remote Sens.* **2016**, *54*, 4501–4512. [[CrossRef](#)]
15. Shibata, A. A wind speed retrieval algorithm by combining 6 and 10 GHz data from Advanced Microwave Scanning Radiometer: Wind speed inside hurricanes. *J. Oceanogr.* **2006**, *62*, 351–359. [[CrossRef](#)]
16. El-Nimri, S.F.; Jones, W.L.; Uhlhorn, E.; Ruf, C.; Johnson, J.; Black, P. An improved C-band ocean surface emissivity model at hurricane-force wind speeds over a wide range of earth incidence angles. *IEEE Trans. Geosci. Remote Lett.* **2010**, *7*, 641–645. [[CrossRef](#)]
17. Zabolotskikh, E.V.; Mitnik, L.M.; Chapron, B. New approach for severe marine weather study using satellite passive microwave sensing. *Geophys. Res. Lett.* **2013**, *40*, 3347–3350. [[CrossRef](#)]
18. Zabolotskikh, E.V.; Mitnik, L.M.; Chapron, B. GCOM-W1 AMSR2 and MetOp-A ASCAT wind speeds for the extratropical cyclones over the North Atlantic. *Remote Sens. Environ.* **2014**, *147*, 89–98. [[CrossRef](#)]
19. Yao, P.; Wan, J.; Wang, J.; Zhang, J. Satellite retrieval of hurricane wind speeds using the AMSR2 microwave radiometer. *Chin. J. Oceanol. Limnol.* **2015**, *33*, 1104–1114. [[CrossRef](#)]
20. Gaiser, P.W.; St. Germain, K.M.; Twarog, E.M.; Poe, G.A.; Purdy, W.; Richardson, D.; Grossman, W.; Jones, W.L.; Spencer, D.; Golba, G.; et al. The WindSat spaceborne polarimetric microwave radiometer: Sensor description and early orbit performance. *IEEE Trans. Geosci. Remote Sens.* **2004**, *42*, 2347–2361. [[CrossRef](#)]
21. Yueh, S.H.; Stiles, B.W.; Tsai, W.Y.; Hu, H.; Liu, W.T. QuikSCAT geophysical model function for tropical cyclones and application to Hurricane Floyd. *IEEE Trans. Geosci. Remote Sens.* **2001**, *39*, 2601–2612. [[CrossRef](#)]
22. Adams, I.S.; Hennon, C.C.; Jones, W.L.; Ahmad, K.A. Evaluation of hurricane ocean vector winds from WindSat. *IEEE Trans. Geosci. Remote Sens.* **2006**, *44*, 656–667. [[CrossRef](#)]
23. Bessho, K.; DeMaria, M.; Knaff, J.A. Tropical cyclone wind retrievals from the Advanced Microwave Sounding Unit: Application to surface wind analysis. *J. Appl. Meteorol. Climatol.* **2006**, *45*, 399–415. [[CrossRef](#)]
24. Zhang, B.; Perrie, W. Recent progress on high wind-speed retrieval from multi-polarization SAR imagery: A review. *Int. J. Remote Sens.* **2014**, *35*, 4031–4045. [[CrossRef](#)]
25. Powell, M.D.; Houston, S.H.; Amat, L.R.; Morisseau-Leroy, N. The HRD real-time hurricane wind analysis system. *J. Wind Eng. Ind. Aerod.* **1998**, *77*, 53–64. [[CrossRef](#)]
26. Houston, S.H.; Shaffer, W.A.; Powell, M.D.; Chen, J. Comparisons of HRD and SLOSH surface wind fields in hurricanes: Implications for storm surge modeling. *Weather Forecast.* **1999**, *14*, 671–686. [[CrossRef](#)]
27. Sampson, C.R.; Schrader, A.J. The automated tropical cyclone forecasting system (version 3.2). *Bull. Am. Meteorol. Soc.* **2000**, *81*, 1231–1240. [[CrossRef](#)]
28. Uhlhorn, E.; Black, P. Verification of remotely sensed sea surface winds in hurricanes. *J. Atmos. Ocean Technol.* **2003**, *140*, 99–116. [[CrossRef](#)]
29. Uhlhorn, E.; Black, P.; Franklin, J.; Goodberlet, M.; Carswell, J.; Goldstein, A. Hurricane surface wind measurements from an operational stepped frequency microwave radiometer. *Mon. Weather Rev.* **2007**, *135*, 3070–3085. [[CrossRef](#)]
30. Klotz, B.W.; Uhlhorn, E.W. Improved stepped frequency microwave radiometer tropical cyclone surface winds in heavy precipitation. *J. Atmos. Ocean Technol.* **2014**, *31*, 2392–2408. [[CrossRef](#)]
31. Yueh, S.H.; Stiles, B.W.; Liu, W.T. QuikSCAT wind retrievals for tropical cyclones. *IEEE Trans. Geosci. Remote Sens.* **2003**, *41*, 2616–2628. [[CrossRef](#)]
32. Hilburn, K.A.; Wentz, F.J. Intercalibrated passive microwave rain products from the unified microwave ocean retrieval algorithm (UMORA). *J. Appl. Meteorol. Climatol.* **2008**, *47*, 778–794. [[CrossRef](#)]
33. Chu, J.H. Tropical Cyclone Forecasters’s Reference Guide. Reference document initially published as NRL Report NRL/PU/7541-95-0012. October 1995. Available online: <http://www.nrlmry.navy.mil/%7Echu/index.html> (accessed on 21 March 2016).
34. Tsang, L. Polarimetric passive microwave remote sensing of random discrete scatterers and rough surfaces. *J. Electromagn. Wave* **1991**, *5*, 41–57.
35. Yueh, S.H.; Kwok, R. Electromagnetic fluctuations for anisotropic media and the generalized Kirchhoff’s law. *Radio Sci.* **1993**, *28*, 471–480. [[CrossRef](#)]

36. Smith, C.K.; Bettenhausen, M.; Gaiser, P.W. A statistical approach to WindSat ocean surface wind vector retrieval. *IEEE Trans. Geosci. Remote Lett.* **2006**, *3*, 164–168. [[CrossRef](#)]
37. Li, L.; Gaiser, P.W.; Gao, B.C.; Bevilacqua, R.M.; Jackson, T.J.; Njoku, E.G.; Rudiger, C.; Calvet, J.C.; Bindlish, R. WindSat global soil moisture retrieval and validation. *IEEE Trans. Geosci. Remote Sens.* **2010**, *48*, 2224–2241. [[CrossRef](#)]
38. Johnson, J.T. An efficient two-scale model for the computation of thermal emission and atmospheric reflection from the sea surface. *IEEE Trans. Geosci. Remote Sens.* **2006**, *44*, 560–568. [[CrossRef](#)]
39. Wentz, F.J. A model function for ocean microwave brightness temperatures. *J. Geophys. Res.* **1983**, *88*, 1892–1908. [[CrossRef](#)]
40. Shibata, A. A change of microwave radiation from the ocean surface induced by air-sea temperature difference. *Radio Sci.* **2003**. [[CrossRef](#)]
41. Ulaby, F.T.; Moore, R.K.; Fung, A.K. *Microwave Remote Sensing Active and Passive-Volume III: From Theory to Applications*; Artech House: Dedham, MA, USA, 1986.
42. Chevallier, F. *Sampled Databases of 60-Level Atmospheric Profiles from the ECMWF Analyses*; Research Report No.4; Eumetsat/ECMWF SAF Programme: Darmstadt, Germany, 2001.
43. Courtier, P.; Andersson, E.; Heckley, W.; Vasiljevic, D.; Hamrud, M.; Hollingsworth, A.; Rabier, F.; Fisher, M.; Pailleux, J. The ECMWF implementation of three-dimensional variational assimilation (3D-Var). I: Formulation. *Q. J. R. Meteorol. Soc.* **1998**, *124*, 1783–1807. [[CrossRef](#)]
44. Wentz, F.J. A well-calibrated ocean algorithm for special sensor microwave/imager. *J. Geophys. Res.* **1997**, *102*, 8703–8718. [[CrossRef](#)]
45. Liebe, H.J.; Hufford, G.A.; Cotton, M.G. Propagation modeling of moist air and suspended water/ice particles at frequencies below 1000 GHz. In Proceedings of the AGARD 52nd Specialists’s Meeting Electromagnetic Wave Propagation Panel, Palma de Mallorca, Spain, 17–21 May 1993.
46. Rosenkranz, P.W. Water vapor microwave continuum absorption: A comparison of measurements and models. *Radio Sci.* **1998**, *33*, 919–928. [[CrossRef](#)]
47. Hocking, J.; Rayer, P.J.; Rundle, D.; Saunders, R.W.; Matricardi, M.; Geer, A.; Brunel, P.; Vidot, J. *RTTOV v11 Users Guide*; NWP-SAF Report; Met. Office: Exeter, UK, 2014.
48. Shibata, A. AMSR/AMSR-E SST algorithm developments—Removal of ocean wind effect. *Italian J. Remote Sens.* **2004**, *30*, 131–142.
49. Sasaki, Y.; Asanuma, I.; Muneyama, K.; Naito, G.; Suzuki, T. Microwave emission and reflection from the wind-roughened sea surface at 6.7 and 18.6 GHz. *IEEE Trans. Geosci. Remote Sens.* **1988**, *26*, 860–868. [[CrossRef](#)]
50. Klein, L.; Swift, C. An improved model for the dielectric constant of sea water at microwave frequencies. *IEEE Trans. Antennas Propag.* **1977**, *25*, 104–111. [[CrossRef](#)]
51. Wentz, F.J.; Spencer, R.W. SSM/I rain retrievals within a unified all-weather ocean algorithm. *J. Atmos. Sci.* **1998**, *55*, 1613–1627. [[CrossRef](#)]

